Available online at www.sciencedirect.com

ScienceDirect

Underground Space 25 (2025) 262–280

www.keaipublishing.com/undsp

Research Paper

Experimental study on large-scale subway station model considering adjustable water and soil pressure

Dongbo Zhou [a,b,*], Yuan Mei [a,b], Xin Ke [a,b], Ziyang Liu [a,b], Wangyang Xu [a,b]

[a] School of Civil Engineering, Xi'an University of Architecture & Technology, Xi'an 710055, China
[b] Shaanxi Key Laboratory of Geotechnical and Underground Space Engineering, Xi'an 710055, China

Received 18 December 2024; received in revised form 23 May 2025; accepted 31 May 2025
Available online 20 September 2025

Abstract

To investigate the structural stress conditions during the excavation and failure stages of subway stations under adjustable water and soil pressures, a 1:10 scaled model was created based on similarity theory. Considering the equivalent soil pressure load, the loading procedures that controlled the excavation and failure of a metro station created via the cover excavation reverse construction method were evaluated. Additionally, an excavation unloading device and an external soil pressure-based graded loading device were developed for a metro station created via the cover excavation reverse construction method. By comparing the experimental results with the finite element simulation results, the axial force variations in the balance props during the excavation process were revealed, and the crack development process of the metro station was summarized. The external soil pressure remained unchanged; furthermore, the increase in the axial force of the balance props was negatively correlated with the distance to the previous balance prop and positively correlated with the axial force of the previous balance prop at the time of unloading. According to the graded soil pressure load and the corresponding crack initiation, development, and structural failure states, the model failure process was divided into four stages: the no-crack stage, initial cracking stage, crack penetration stage, and local damage stage. The first cracks in the station structure appeared at the corners and centers of the excavation openings. The first penetration of transverse cracks appeared in the middle of the basement first-floor wall. The cracks at the excavation opening corners and middle locations developed obliquely, forming an overall horseshoe shape. Localized damage first occurred at the corners where concrete spalled, exposing the reinforcement.

Keywords: Water and soil pressure; Cover excavation reverse construction; Loading device design; Model experiment; Finite element simulation

1 Introduction

In the cover excavation reverse construction method, road traffic can be promptly restored after the creation of the cover slab is completed, reducing both the area and duration of road occupation during the construction process (Jamsawang et al., 2017). Compared with traditional steel and concrete supports, closed slabs have higher overall rigidity, serving as lateral supports that better control ground settlement and sidewall deformation caused by excavation (Chen et al., 2021). This approach effectively increases the safety of foundation pit excavation. Consequently, the use of the cover excavation reverse construction process in foundation pit projects in urban centers is increasingly common (Mei et al., 2024; Meral et al., 2024). During the excavation of subway stations, continuous changes in ground overload lead to dynamic variations in the lateral earth pressure at the main station structure, which results in significant safety risks to the construction and operation of the station (Zhou et al., 2024).

Current research has focused primarily on the impact of the cover excavation reverse construction method on the deformation of the surrounding soil and adjacent structures and buildings (Guo et al., 2022; Sun et al., 2022; Wang et al., 2024a). However, research on the stress

* Corresponding author at: School of Civil Engineering, Xi'an University of Architecture & Technology, Xi'an 710055, China.
E-mail address: zdb@xauat.edu.cn (D. Zhou).
Peer review under the responsibility of Tongji University

https://doi.org/10.1016/j.undsp.2025.05.007

states of structures during the construction and operation of subway stations created via the cover excavation reverse construction method is limited. Experimental methods are critical in engineering to evaluate structural stress behavior. In situ experiments can comprehensively reflect the combined effects of factors such as the geology, construction method, and surrounding environment of a subway station (Xu et al., 2024; Xue et al., 2024). However, construction site environments are complex, and conducting long-term tests after setting up the testing instruments can easily affect the construction progress. Additionally, various types of construction loads exist onsite, making it difficult for in situ experiments to provide intuitive experimental data for the issues being analyzed. Model experiments can be conducted to simplify structures on the basis of the research object and to improve or design loading devices based on the research findings. The application of these methods in structural performance analysis is gradually increasing. Typical model experiments include centrifuge experiments (Ma & Cao, 2024) and 1*g* scaled model experiments (Jin et al., 2024). However, the space for arranging loading devices and testing instruments is limited in centrifuge experiments; thus, considering the subway station size and centrifuge model box size, it remains difficult to replicate the construction and failure processes of underground structures with such models. Traditional 1*g* scaled model box experiments involve constant soil pressure, making it difficult to reflect the changes in soil pressure caused by ground surface overloading. Therefore, the development of large-scale subway station models with adjustable soil–water pressures is highly important for analyzing the structural stress characteristics of subway stations under different overload conditions. Static loading experiments are based on predetermined loads and displacements, and they involve applying slow loading to the experimental model to replicate the elastic, elastoplastic, plastic, and failure working states of the structure throughout its lifecycle. Such methods are widely used in above-ground structural model experiments (Elbelbisi et al., 2024; Vuong et al., 2023). Ma and Liu (2023), Ganesh and Ramachandra Murthy (2023), Zhou et al. (2023), LeBlanc et al. (2024), and others have studied the concrete strain, ultimate load capacity, and failure modes of engineered cementitious composites (ECC)-reinforced beams, ultra-high performance concrete (UHPC)-reinforced beams, fiber-reinforced polymer reinforced beams, and modular polymer columns. As building structures become increasingly complex, joints experience multiple stress states, such as tension, bending, and torsion, leading to increased safety risks. For example, Pham et al. (2024) researched the tensile load capacity and failure mechanisms of prefabricated beam column structures. Moreover, Wang et al. (2024b) studied the mechanical properties, stiffness degradation patterns, and failure modes of double-layer steel tube concrete columns and reinforced concrete beam column joints and proposed reinforcement measures for the joints.

However, component and joint experiments often fail to reflect the overall load-bearing characteristics and failure modes of engineering structures. Several large-scale loading devices for analyzing the overall load states of structural models have been developed (Wang et al., 2022; Zhang et al., 2024; Zhuang et al., 2021). However, owing to the complexity of geological conditions, loads, and boundary conditions in underground structures, current research is focused primarily on the interactions between underground structures and soils in model box experiments, with relatively few studies focusing on static loading devices for underground structures (Fu & Li, 2020; Zhang et al., 2022). Considering the difficulty and cost of designing, manufacturing, and assembling such devices, few models can intuitively simulate the increase in active soil pressure caused by changes in the overlying soil load. On the basis of existing research and equivalent soil pressure loads, we design, manufacture, and assemble excavation unloading devices for cover excavation reverse subway station pits and external soil pressure-based graded loading devices. Furthermore, a loading protocol for the excavation and failure of subway stations created via the cover excavation reverse method is established, experimental tests are conducted, and the initiation, development, and local failure processes of cracks in subway stations under adjustable water and soil loads are analyzed. Furthermore, on the basis of finite element simulation results, we demonstrate the feasibility of the adjustable water and soil pressure subway station model, suggesting that this model may serve as a viable experimental testing method for studying the excavation–failure–failure processes of subway stations. This research provides a new experimental loading device and testing scheme for failure analysis in similar underground engineering structures.

2 Conceptual design of the model experiments

We select a Guangzhou subway station created via the cover excavation reverse construction method as the engineering base and consider a typical section of the prototype station. Then, by considering the expected size of the loading device and the available laboratory space, we determine the scaling ratio of the model. On the basis of the basic similarity ratios of the geometric dimensions, material density, and elastic modulus, the scaling ratios for the model loads and material properties are derived. Additionally, on the basis of the theory of equal bearing capacity, the reinforcement of the scaled model is calculated. On this basis, the model is constructed, and the arrangement of testing instruments is implemented.

After the model is constructed, external reaction beams are used to provide soil pressure to the distribution beams. The soil pressure load is calculated on the basis of the geological conditions of the prototype structure and the physical and mechanical parameters of the soil. Considering the equivalence of soil pressure loads, hydraulic equipment is connected to the jacks and applied to the distribution

beams to simulate stratified and layered soil pressures. Outer steel plates are installed on the outside of the scaled model, and sand is filled between the model and the steel plates to simulate the interaction between the structure and the soil. Additionally, counterweights are placed on top of the structure to simulate the overlying load. Inside the structure, layered soil pressure balance props (hereinafter referred to as balance props) are set up to simulate the internal soil. The balance props are progressively removed in layers to simulate the excavation process of the foundation pit of the station.

The loading process and regime are established on the basis of the experimental design plan. Various experimental phenomena are recorded during each stage, and the rationality and effectiveness of the experimental approach are verified by comparing the results with those of numerical simulations. The initiation and development of structural cracks are analyzed, the structural failure patterns are studied, and the shortcomings and limitations of the experimental plan are discussed. The design concept of the experimental plan is shown in Fig. 1.

3 Model experimental design and production

3.1 Prototype structure

The subway station constructed using the cover excavation reverse construction method is a four-level underground island-style station with a single-column double-span structure. The station has a length of 166.65 m, with a standard section width of 24.5 m and an overall height of 26.6 m. The overburden thickness above the station is 6.5 m. From top to bottom, the soil layers at the station include miscellaneous fill, silty soil, fine silty sand, and other soil types. The typical elevation and soil distribution of the test area are shown in Fig. 2.

3.2 Model structure

3.2.1 Model dimensions

The width of the standard section of the prototype station structure is 24.5 m, and the spacing between individual channels in the laboratory is 2.1 m. Considering

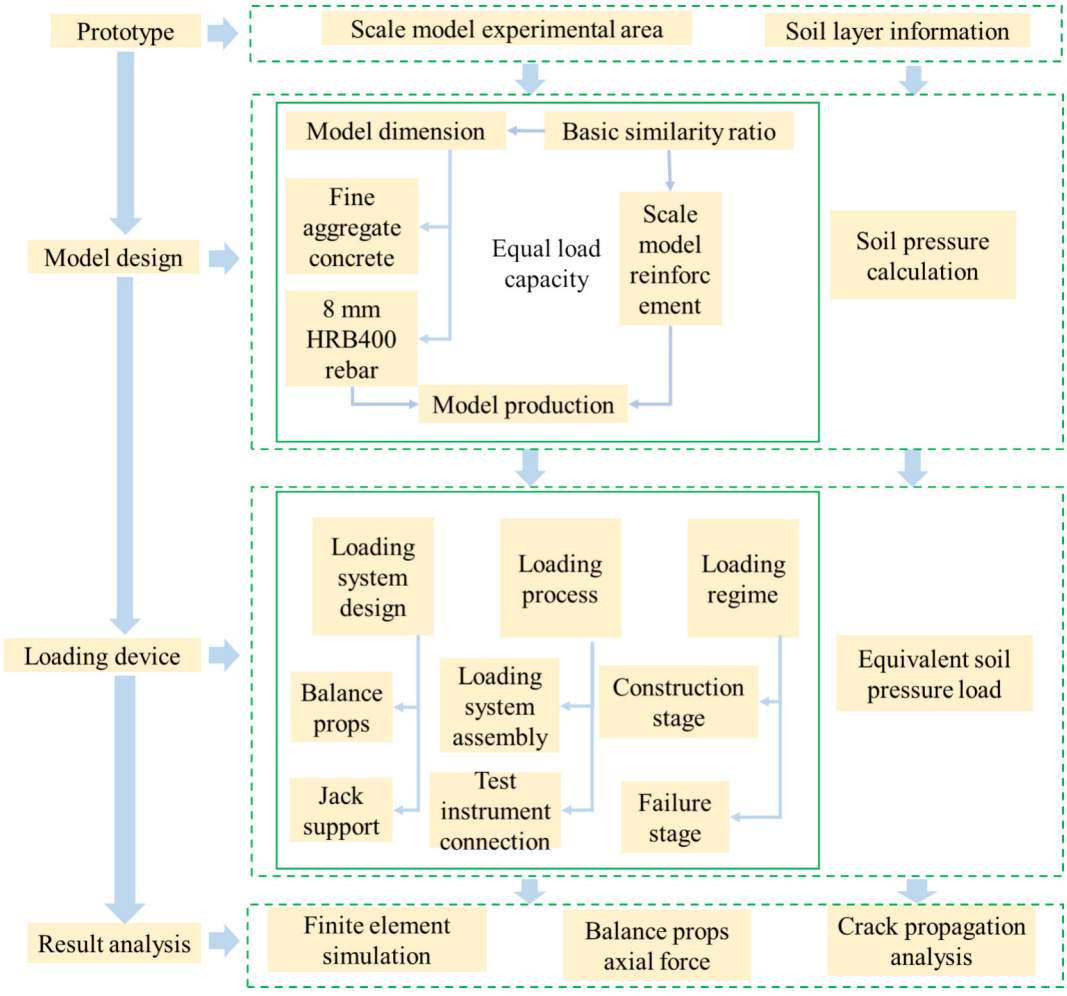

Fig. 1. Experimental plan design concept.

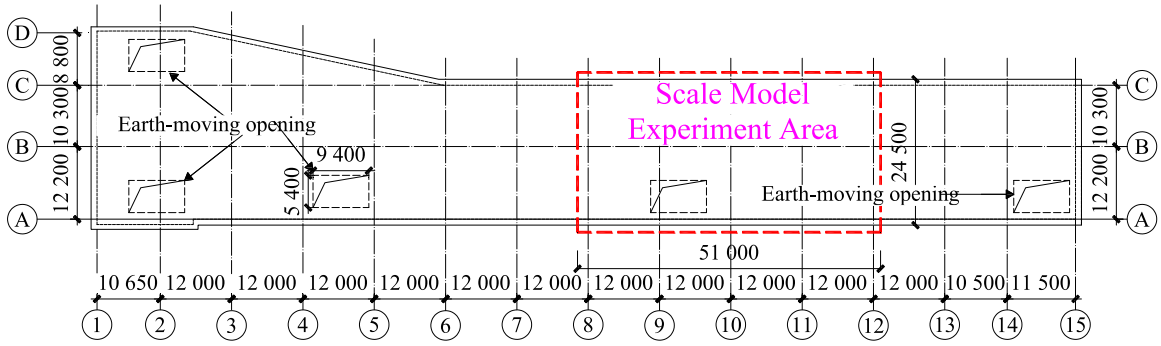

(a)

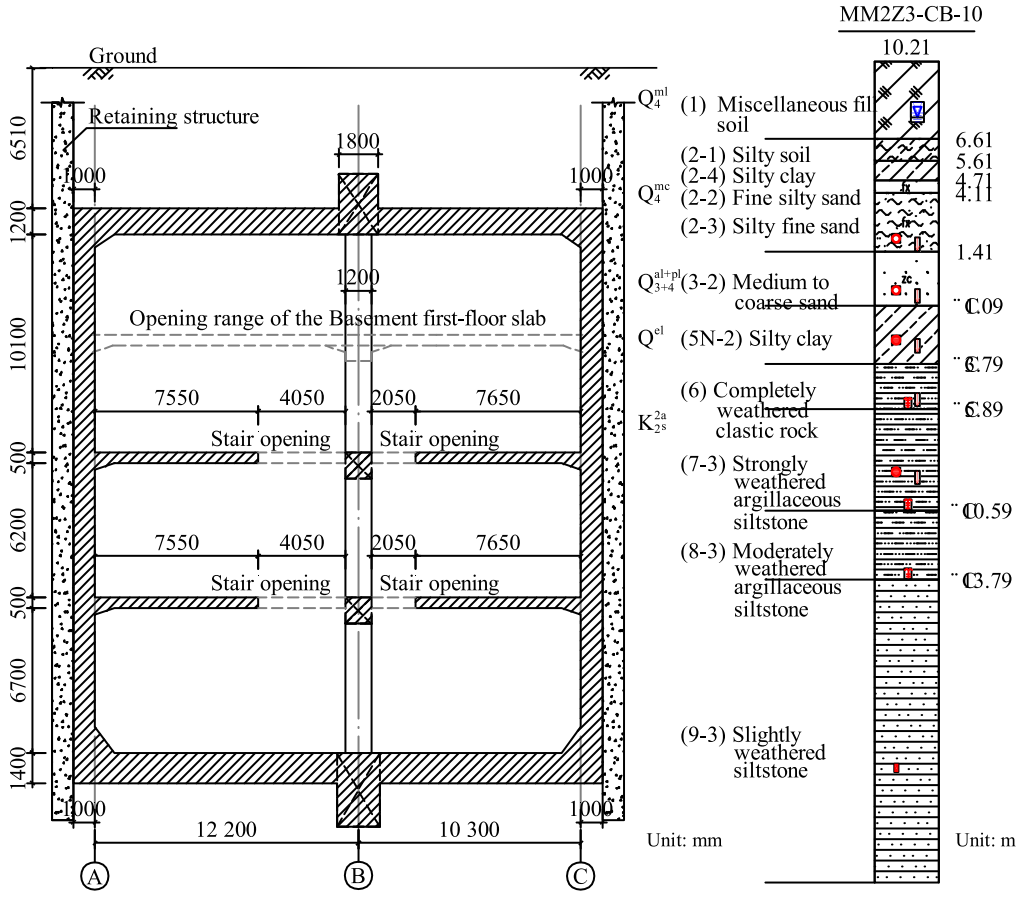

(b)

Fig. 2. Prototype and soil layer information. (a) Plan of the experimental area, and (b) elevation of the experimental area and distribution of soil layers.

the spacing of the support frame arrangements, loading device dimensions, model structure dimensions, and available laboratory space, the scale ratio of the scaled model is set as 1:10. The model is constructed using axes 8–12 of the prototype station as the reference. The three-dimensional dimensions of the model are 5.10 m × 2.45 m × 2.52 m (length × width × height).

3.2.2 Materials

The model is made with fine aggregate concrete, with a maximum aggregate particle size of less than 15 mm. The concrete strength is consistent with that of the prototype structure. The steel pipe columns are filled with C60 fine aggregate concrete, whereas the other model components are made with C35 fine aggregate concrete. During the model fabrication process, standard 150 mm × 150 mm × 150 mm cubic test blocks are produced for compressive strength testing. The concrete cube compressive strength test is shown in Fig. 3. HRB400 steel bars are used in the model, and Q235 steel is used for the steel pipe piles. The outer diameter of the steel pipe piles is 1200 mm, with a wall thickness of 35 mm. The material properties

Fig. 3. Concrete cube compressive strength test.

of the rebars and steel tubes are listed in Tables 1 and 2.

3.2.3 Similarity theory

In accordance with the Buckingham–π theorem, similarity ratios for the subway station model dimensions are calculated with the geometric dimensions, material density, and elastic modulus as the fundamental physical quantities (Marzec & Tejchman, 2022; Shi et al., 2024). Table 3 presents a summary of the similarity ratios for the scaled model.

3.3 Model reinforcement and arrangement

3.3.1 Model reinforcement calculation

The reinforcement calculation for the scaled model follows the equivalent bearing capacity principle (Sun et al., 2023; Wang et al., 2024b). The calculation of the reinforcement area for the beams, slabs, and columns follows the equivalent bending capacity principle, whereas the calculation of the stirrup area follows the equivalent shear capacity principle.

3.3.2 Reinforcement arrangement

WZL1, 2ZZL1, and 3ZZL1 represent the main beams of the roof slab, the second-basement slab, and the third-basement slab, respectively, whereas the other beams are secondary beams. To distinguish the main beams, secondary beams, and intermediate columns, each beam and column is numbered sequentially. The numbering sequence and scaled dimensions of the subway station model structure are shown in Fig. 4 (Zhou et al., 2024). In the figure, all dimension annotations are in millimeters, except for the elevation, which is in meters.

3.4 Model fabrication and sensor bonding

On the basis of the scaled model dimensions, reinforcement calculations, and measurement point layouts, and in conjunction with the actual construction process, model fabrication and sensor bonding are carried out. Cushion blocks are placed on top of the formwork, with the thickness of the cushion blocks corresponding to the cover thickness. The beam rebar cages for the floor slab are produced according to the design and placed inside the beam formwork. The steel pipe, concrete, and slab joint locations

Table 1
Rebar material parameters.

Material	Diameter (mm)	Yield strength (MPa)	Tensile strength (MPa)	Elastic modulus (MPa)
HRB400	8	525	671	2.10×10^5

Table 2
Steel tube material parameters.

Material	Thickness (mm)	Yield strength (MPa)	Tensile strength (MPa)	Elastic modulus (MPa)
Q235	3	252	413	2.15×10^5

Table 3
Similarity ratios of the scaled model.

Similarity parameters	Physical quantity	Dimension	Similarity relationship	Similarity ratio (model:prototype = 1:10)
Geometric parameters	Length L	[L]	S_l	0.1
	Area A	[L^2]	$S_s = S_l^2$	0.01
	Linear displacement μ	[L]	$S_\mu = S_l$	0.1
Material parameters	Elastic modulus E	[FL^{-2}]	S_E	1.0
	Stress σ	[FL^{-2}]	$S_\sigma = S_E$	1.0
	Strain ε	–	$S_\varepsilon = 1$	1.0
Load parameters	Concentrated force F	[F]	$S_F = S_E S_l^2$	0.01
	Linear load ω	[FL^{-1}]	$S_w = S_E S_l$	0.1
	Surface load q	[FL^{-2}]	$S_q = S_E$	1.0
	Moment M	[FL]	$S_M = S_E S_l^3$	0.001

are reinforced with rebar anchoring. The model fabrication and strain gauge attachment processes are as follows:

(1) Model fabrication: rebar bending → wooden wedge ground leveling → formwork erection → rebar laying

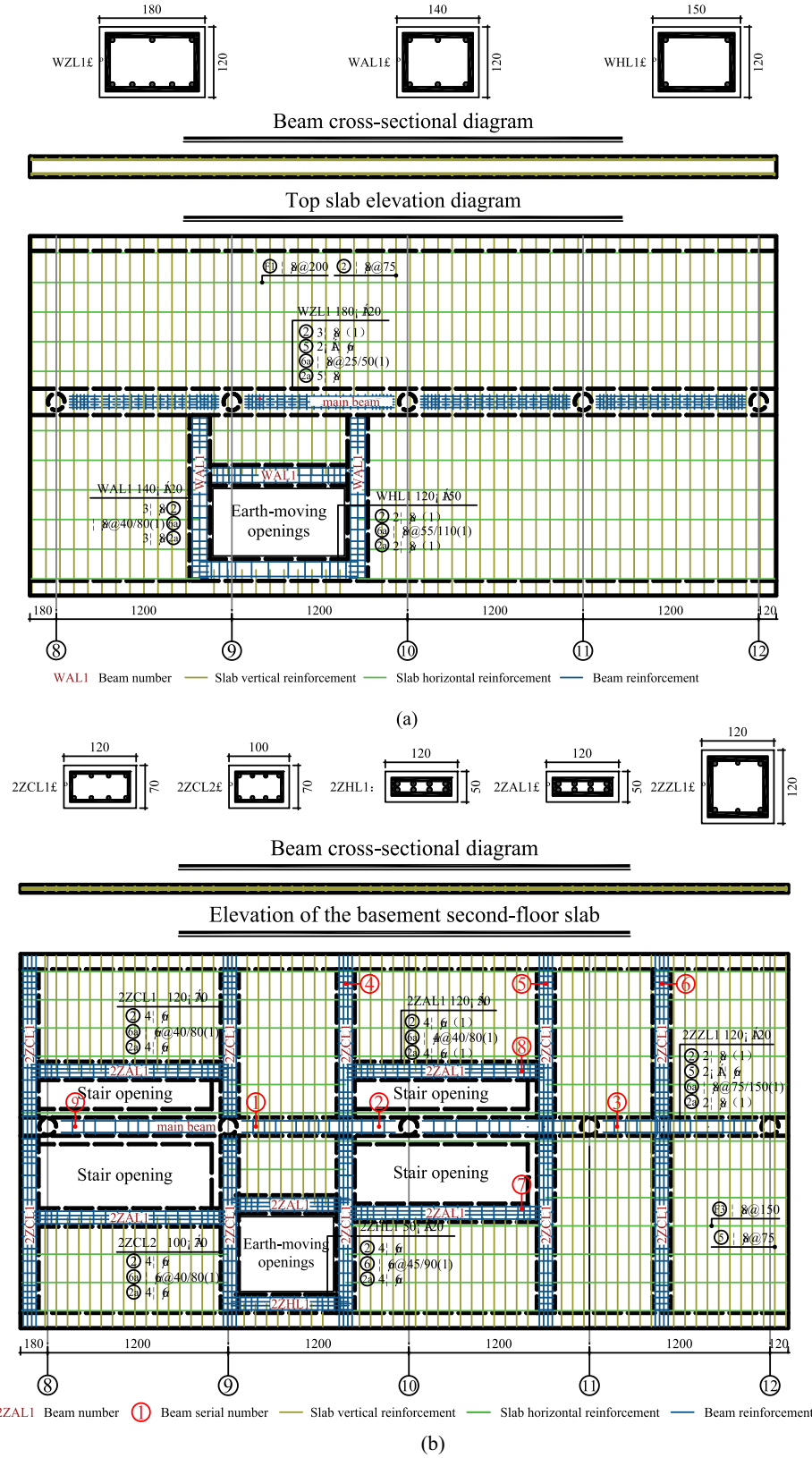

Fig. 4. Model reinforcement diagram. (a) Top slab reinforcement, (b) reinforcement of the basement second-floor slab, (c) reinforcement of the basement third-floor slab, and (d) wall reinforcement. (Unit: mm)

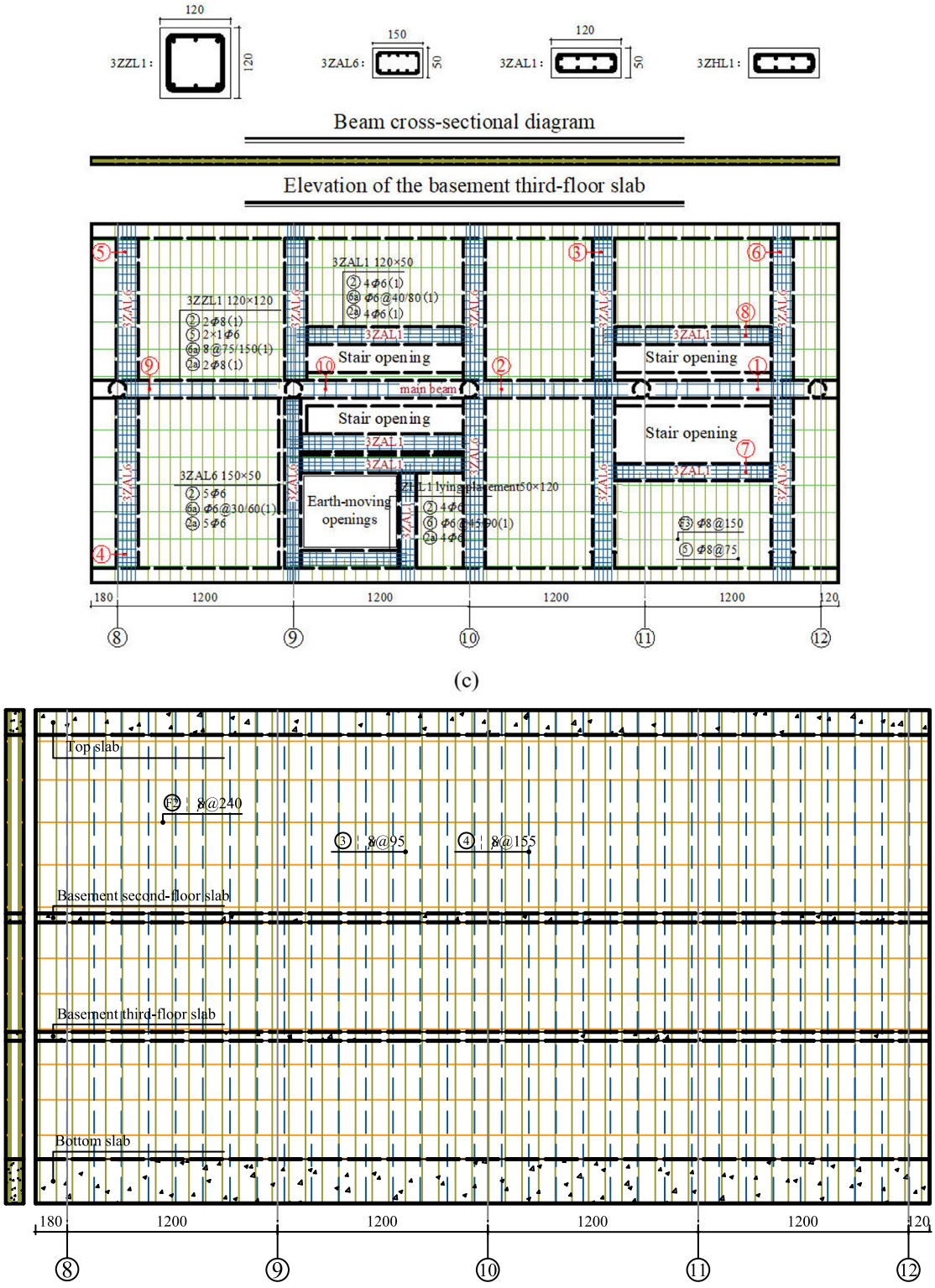

Fig 4. *(continued)*

→ concrete pouring, compaction, and curing → bottom layer, basement third floor, basement second floor, and roof model construction.

(2) Strain gauge bonding on the rebar: measurement point location → rebar grinding → strain gauge bonding → conductivity testing → gauze wrapping with epoxy.

After the model was fabricated, the concrete strain gauges and steel pipe strain rosettes were bonded. To observe the model failure process, gypsum powder is applied to the surface of the structure, and chalk lines are snapped every 5 cm using a chalk line reel to create a square grid. Figure 5 illustrates the model fabrication process.

4 Loading scheme

4.1 Calculation of hydrostatic and soil pressures

When conducting model experiments for underground structures, the calculation and simulation of hydrostatic and soil pressures are crucial. The burial depth and soil layer distribution of the prototype structure are shown in Fig. 6. The soil pressure is calculated on the basis of Rankine's active earth pressure theory via a method that separates the calculations of the hydrostatic and soil pressures (Du et al., 2024; Du et al., 2022). The pressure is calculated according to Eq. (1), and the resulting soil pressure is computed according to Eq. (4).

$$p = K_a\gamma' z - 2c\sqrt{K_a} + \gamma_w z, \tag{1}$$

$$K_a = \tan^2\left(45 - \frac{\phi}{2}\right), \tag{2}$$

$$E_a = \frac{1}{2}K_a\gamma' h^2, \tag{3}$$

$$E_a = \frac{1}{2}(h - z_0)\left(\gamma h K_a - 2c\sqrt{K_a}\right), \tag{4}$$

where p is the total active earth pressure intensity (kPa); γ' is the unit weight of the soil (kN/m^3); γ_w is the unit weight of water, which is taken as 9.8 kN/m^3 in this paper; z is the depth of the soil layer (m); h is the thickness of each soil layer (m); K_a is the Rankine active earth pressure coefficient; ϕ is the internal friction angle of the soil. The prototype station is buried at a depth of 6.8 m. The station model simultaneously considers surface overloading, vehicle loads, and crowd loads, and the calculated load distribution is shown in Fig. 6.

The 25.2-m-high station structure is divided into three soil layers. The total hydrostatic and soil pressures for each layer are 999.41, 1819.24, and 2854.65 kN/m. The hydrostatic and soil pressures are multiplied by the model length of 5.1 m to obtain the corresponding concentrated loads for the station structure. After scaling, the corresponding concentrated loads are 50.97, 92.78, and 145.59 kN. These

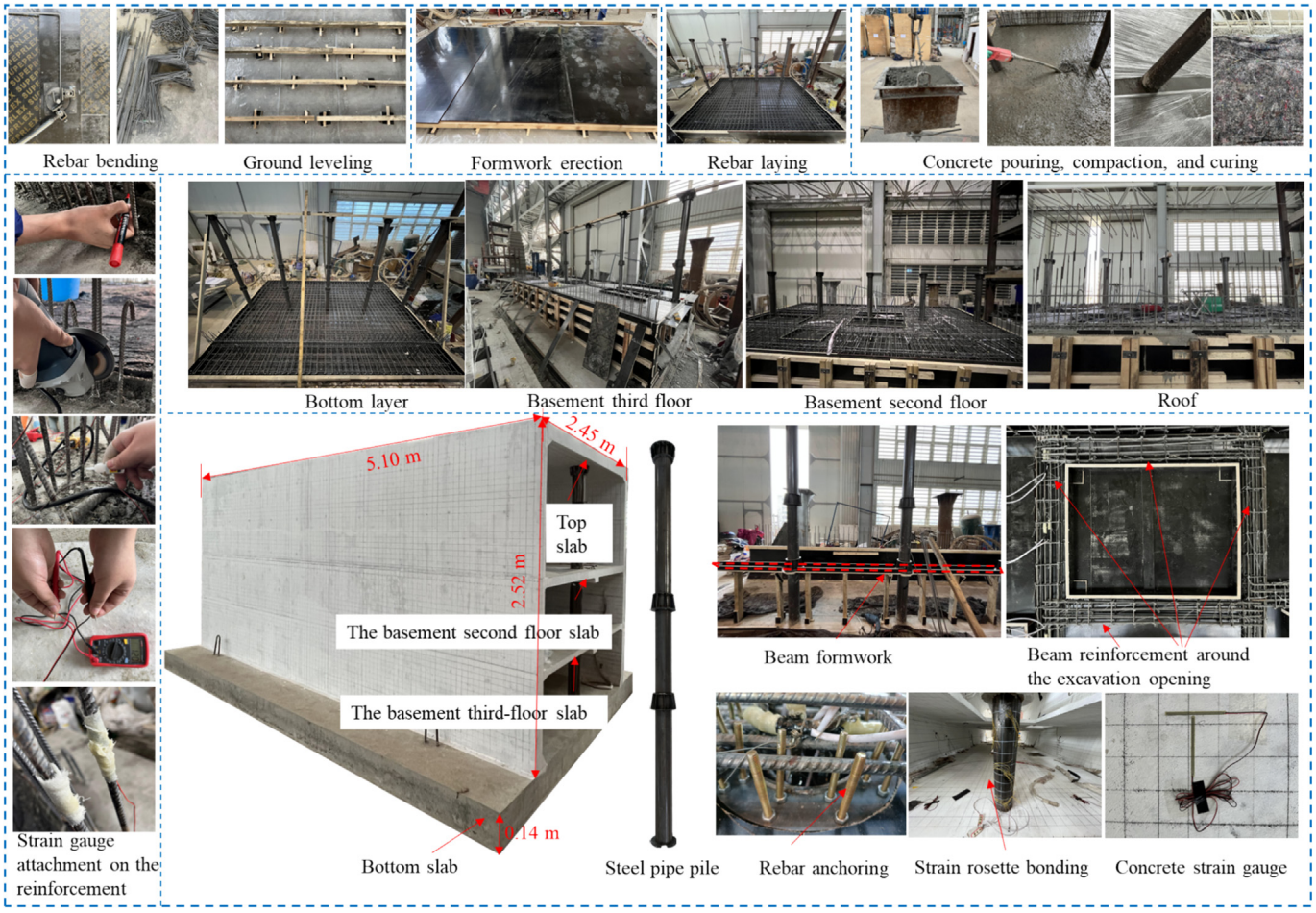

Fig. 5. Model fabrication.

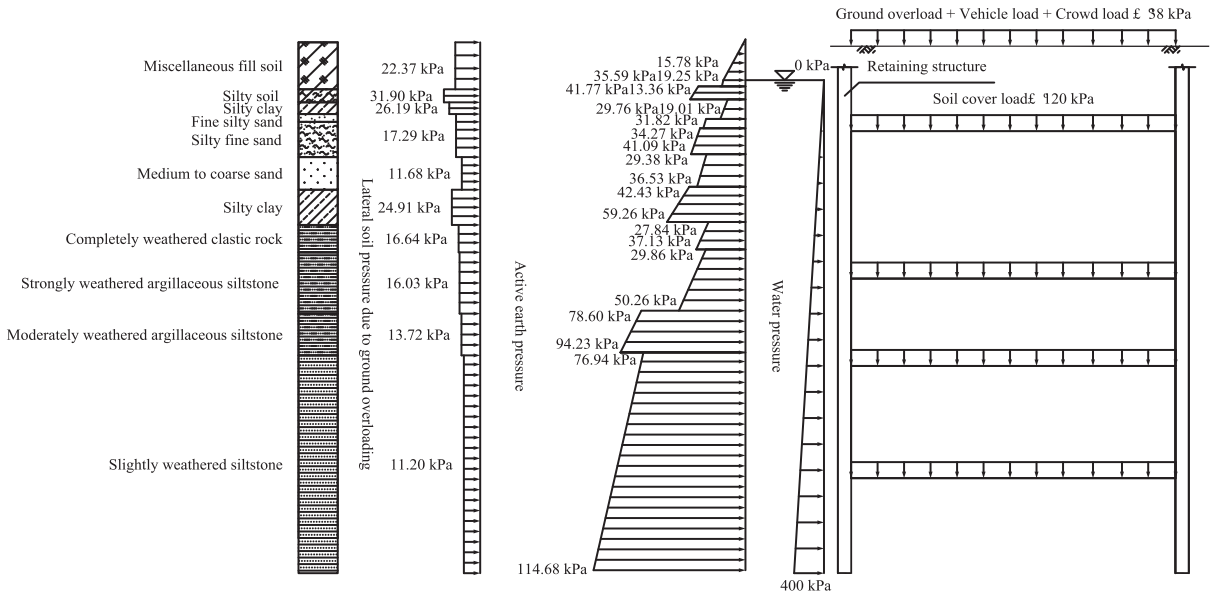

Fig. 6. Load distribution.

Table 4
Calculated soil layer loads.

Soil layer name	Range of burial depth for each soil layer (m)	Soil layer thickness (m)	Soil layer thickness (m)	Hydrostatic and soil pressure (kN/m)	Concentrated load (kN)	Scaled concentrated load (kN)	Load of each jack for each layer (kN)
Silty fine sand	6.81 8.80	1.99	8.4	170.41	5096.99	50.97	16.99
Medium to coarse sand	8.80 11.0	2.50		257.56			
Silty clay	11.3 14.0	2.70		395.25			
Completely weathered clastic rock	14.0 15.2	1.21		176.18			
	15.2 16.1	0.89	8.4	142.08	9278.12	92.78	30.93
Strongly weathered argillaceous siltstone	16.1 20.8	4.70		904.51			
Moderately weathered argillaceous siltstone	20.8 23.6	2.81		772.66			
	23.6 24.0	0.39	8.4	115.39	14 558.72	145.59	48.53
Slightly weathered siltstone	24.0 32.0	8.01		2739.26			

concentrated loads are applied by three jacks, with the calculated concentrated loads for each jack being 16.99, 30.93, and 48.53 kN. Table 4 shows the calculation results for the soil layer loads.

4.2 Design and installation of the loading experimental device

4.2.1 Jack support design

To facilitate the placement and adjustment of the jacks during the experimental phase, a jack support is designed. The jack is placed inside the support, and the jack support is positioned at the designated location according to the design plan. To ease the installation of the jack, the radius of the jack support is slightly larger than the radius of the jack. The jack radius is $r = 118$ mm, and the support radius is $R = 120$ mm. To ensure the stability of the jack during loading, once the jack is placed at the designated position, it is fixed with a clamp. The designs of the jack and jack support are shown in Fig. 7(b).

4.2.2 Structure soil interface interaction

To simulate the interface interaction between the station model and soil, a 20-mm-thick steel plate is wrapped

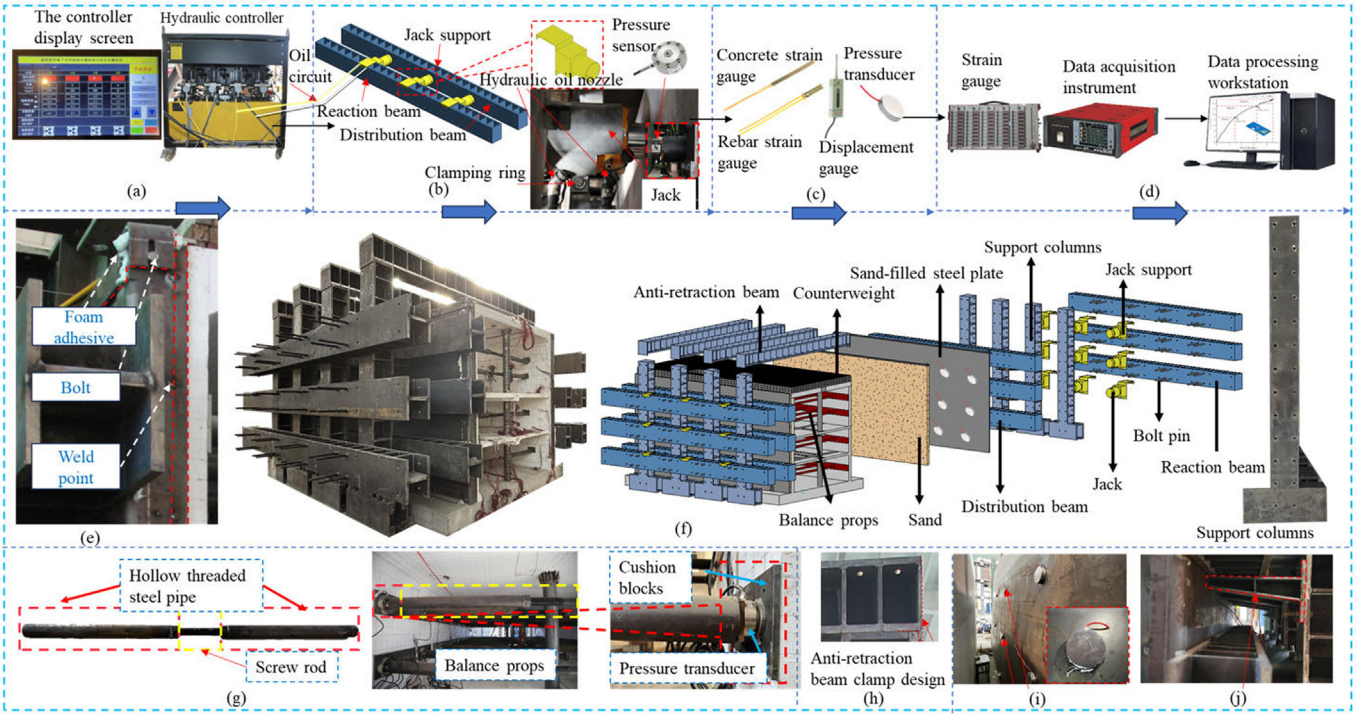

Fig. 7. Loading system design and installation. (a) Control system, (b) loading system, (c) testing instrument, (d) acquisition instrument, (e) the edge sealing structure, (f) load system decomposition diagram, (g) balance props, (h) anti-retraction beam clamp design, (i) pressure sensor arrangement, and (j) steel brackets.

around the outer side of the model structure. A 70-mm-thick gap is left between the model structure and the steel plate. The sand is then filled and compacted in layers beneath the model structure. To prevent the sand from spilling, an edge sealing structure is designed. The steel plate is connected to both sides of the model structure and the top plate with bolts, and the connection between the steel plate and the model structure is further reinforced by spot welding. Finally, foam adhesive is used to fill the microgaps between the steel plates. The design of the edge sealing structure is shown in Fig. 7(e).

4.2.3 Balance prop design

The balance props are designed to simulate the unloading process of the excavation pit. The balance props consist of hollow threaded steel pipes at both ends, with a screw rod in the middle. Four layers of balance props are evenly arranged from top to bottom according to the model height, with each layer consisting of 10 balance props spaced uniformly. During the experiment, a torque wrench is used to tighten or loosen the balance props. To prevent stress concentration at both ends of the balance props, steel plates are placed on both sides of the props, and a pressure sensor is installed at one end of the balance props to measure the real-time axial force. The design of the balance props is shown in Fig. 7(g).

4.3 Loading procedure

This experiment was conducted at the Structural Engineering and Seismic Research Laboratory of Xi'an University of Architecture and Technology, China. The loading equipment was designed, manufactured, and installed according to the loading plan. The model testing procedure is as follows:

(1) Counterweights are placed on the top slab of the model.
(2) Support columns are installed within the laboratory channel and fixed in position using ground anchor bolts. Bolt holes with a diameter of 30 mm are drilled at intervals of 250 mm between the support columns. To ensure the rigidity of the support columns, 16-mm-thick steel rib plates are welded at 250-mm intervals between the columns, as shown in Fig. 7(f).
(3) Sand-filled steel plates are erected on the outside of the model, with the steel plates being 10-mm thick and placed 70 mm away from the model. The steel plates are first secured on both sides with bolts. The dried sand is then filled in layers from top to bottom. After the unit is filled with sand, the top sand-filled steel plate is connected, and the gap between the steel plate and the structure is checked. Foam adhesive is

used to seal the gap. Small holes are made in the sand-filled steel plate for pressure sensor wiring. Three layers of sensors are evenly arranged along the length of the steel plate from top to bottom, with 6 sensors in each layer, totaling 18 pressure sensors, as shown in Fig. 7(i).

(4) Bolt holes on the support columns are connected using bolt nails, with the outer side connected to the reaction beam and the inner side connected to steel brackets (Fig. 7(j)). After the connections are completed, the bolts are tightened to secure the positions of the steel brackets and the reaction beam.

(5) Three layers of jack supports are placed on the reaction beam from top to bottom, with the jacks lifted and installed in each layer. Each layer of jacks is connected in series through a diverter valve, and 3 jacks with a capacity of 200 t are arranged on both the left and right sides of each layer.

(6) A distribution beam is mounted on the steel bracket, with pressure sensors suspended at the jack positions. A hydraulic controller is used to adjust the jacks so that they press against the pressure sensors. The thrust of each layer of jacks is calculated on the basis of the magnitude of the original soil pressure. The jacks push the distribution beam, which evenly distributes the soil pressure along the length of the structure.

(7) Anti-retraction beams are installed at both ends of the support columns. To prevent displacement at the top of the support columns during loading, a clamping plate is designed at the lower part of the anti-retraction beam, as shown in Fig. 7(h).

(8) After the external loading system is arranged, the jacks are connected to the hydraulic controller. The force applied by each layer of jacks is monitored by reading the pressure sensors at the front end of the jacks and the display screen of the controller. Figure 7 (a) shows the control system.

(9) Inside the model, the balance props are arranged sequentially from top to bottom. On the basis of the soil pressure, the pressure values of the balance props are adjusted according to the readings from the pressure sensors at the ends of the balance props.

(10) After the concrete strain gauges, rebar strain gauges, displacement meters, and pressure sensors are numbered, they are connected to the data acquisition device. A data processing workstation is used to analyze the collected data. The testing instruments and data acquisition setup are shown in Fig. 7(c) and (d). The overall design and installation of the loading system for the experiment are shown in Fig. 7.

4.4 Loading regime

On the basis of the load calculation results mentioned above, the model experiment loading process is divided into the construction phase and the bearing capacity phase, with distinct loading protocols. As shown in Fig. 8, the loading steps are as follows:

(1) On the basis of the soil pressure calculation results, a symmetrical load of 1.0 times the soil pressure is applied on both sides of the structure. After the load is applied, the load is held for 10 min to allow the load to stabilize, simulating the excavation of the foundation pit. The experimental phenomena are observed and recorded.

(2) The staged excavation process of the foundation pit is simulated by sequentially removing the balance props in the first, second, third, and fourth layers. After the load is removed from each layer, the load in the other

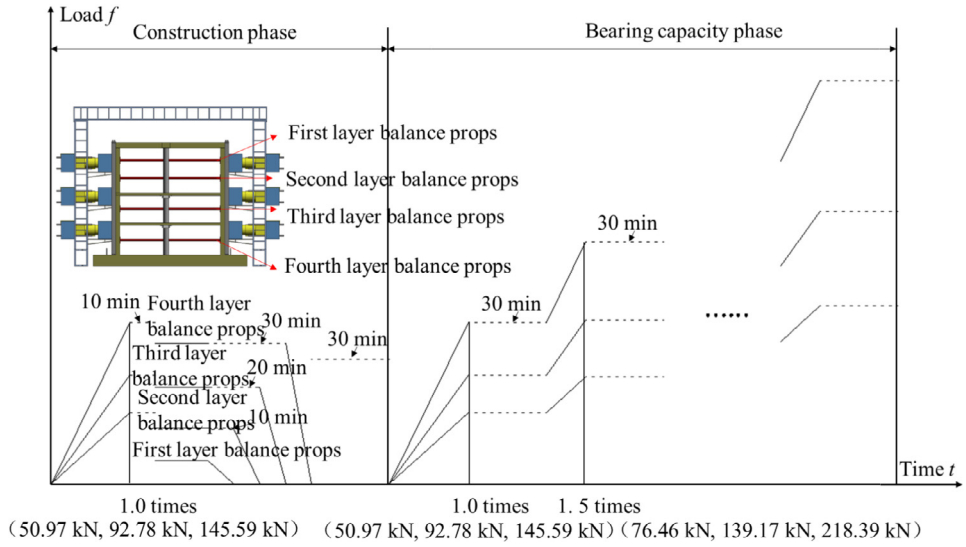

Fig. 8. Loading regime.

layers is held for 10 min to allow the system to stabilize. The experimental phenomena are observed and recorded.

(3) The above process simulates the foundation pit excavation process, namely, the construction phase for a station created via the cover excavation reverse construction method.
(4) The external jacks are unloaded. After unloading, a symmetric load of 1.0 times the soil pressure is applied on both sides of the structure from top to bottom. Once the load is applied, the load is held for 30 min. The experimental phenomena are observed and recorded.
(5) A symmetric load of 1.5 times the soil pressure is applied on both sides of the structure from top to bottom. Once the load is applied, the load is held for 30 min. The experimental phenomena are observed and recorded.
(6) On the basis of experimental processes in steps (4) and (5), staged loading is applied until multiple cracks develop and local damage occurs.

5 Validation of the structural response in cover excavation reverse construction: combined numerical and experimental analysis

To verify the feasibility of the model experiment proposed in this work, a corresponding finite element model is established, as shown in Fig. 9(a) and (b). The bottom of the station is placed on the ground and is constrained by loading devices and spacers at both ends during the experiment, with fixed constraints applied to the bottom. The overlying soil pressure is applied as a uniformly distributed load on the top slab of the structure, and the lateral soil pressure is applied to the distribution beam, with the load application positions and magnitudes consistent with those in the experiment. In the finite element simulation, the bottom slab is set with fixed constraints. Frictional contact is applied between the steel plate and sandy soil and between the sandy soil and concrete, with friction coefficients set as $\mu = 0.6$ and $\mu = 0.55$, respectively (Zhang, 2024; Zhang et al., 2021). A rigid connection is used between the distribution beam and the steel plate. The concrete is modeled via a plastic damage constitutive model (Zhang et al., 2025), with the model parameters listed in Table 5. In the finite element model, a hexahedral-dominated mesh with supplementary tetrahedral elements is utilized. The concrete mesh size along the length direction is 0.05 m. The top slab mesh is divided into 4 layers, including the basement second-floor and basement third-floor slabs, and the sidewall mesh is divided into 3 layers along the thickness direction. The elastic modulus of the rebar is 210 GPa, and the Poisson's ratio is 0.28. The rebar is modeled using embedded truss elements, with mesh lengths of 0.1 m. The elastic modulus of the steel plate is 210 GPa, and the Poisson's ratio is 0.2 (Chang et al., 2022; Zheng et al., 2023).

6 Finite element results analysis

6.1 Analysis of the axial force in the balance props

During the foundation pit excavation simulation phase, no cracks are observed in the station structure; however, the axial forces of the balance props vary. Figure 10 shows the variation in the axial forces of the balance props during the foundation pit excavation simulation. Since the unloading of the balance props is not completed instantaneously, there are slight fluctuations in the measured data. To better illustrate this phenomenon, the numerical simulation results and measured results are presented separately. The figure shows that the measured values are similar to the numerical simulation results, which verifies the accuracy of the simulation method. The unloading of the balance props corresponds to the excavation of the metro station soil. s_{ij} represents the axial force, s represents the balance prop, i (i = 1, 2, 3, 4) represents the layer of the balance prop; and j ($j = 0, 1, \cdots, 9$), represents the sequence of the balance

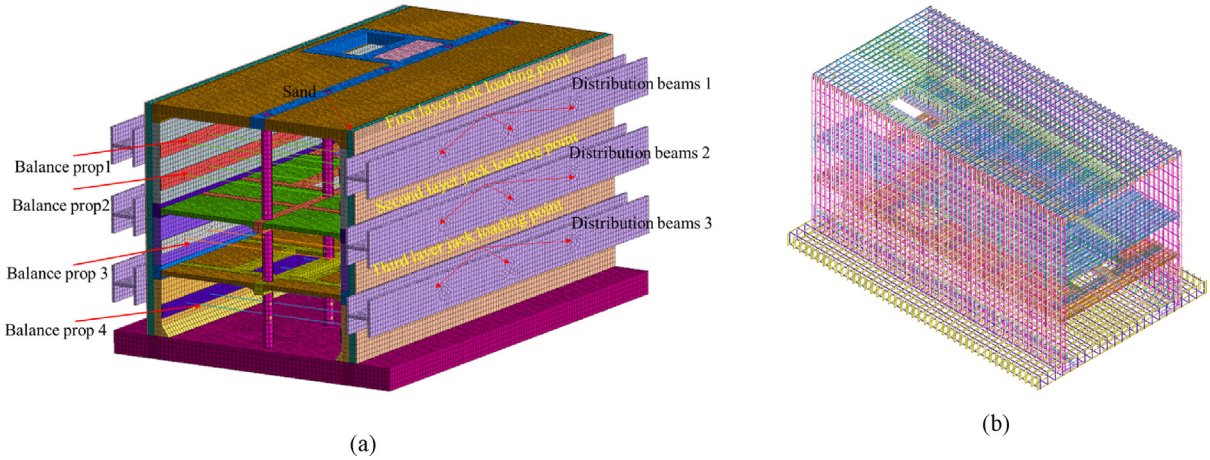

Fig. 9. Finite element model. (a) Main structure, and (b) rebar model.

Table 5
Plastic damage constitutive parameters.

Density ρ (kg/m^3)	2400	Initial compressive yield stress (MPa)	12.85
Poisson's ratio υ	0.2	Tensile stiffness recovery parameter w_t	1.0
Angle of dilation ψ (°)	32.0	Compressive stiffness recovery parameter w_c	0.0
Elastic modulus E (MPa)	31 500	Tensile damage d_t	As shown in Table 6
Initial tensile yield stress (MPa)	2.23	Compressive damage d_c	As shown in Table 7

Table 6
Tensile damage parameters.

Compressive stress (MPa)	12.85	17.97	19.81	23.49	19.32	14.43	9.59	6.69	5.79
Plastic strain (%)	0	0.013	0.020	0.078	0.183	0.291	0.459	0.651	0.745
Damage factor d_c	0	0.064	0.087	0.238	0.471	0.654	0.818	0.901	0.924

Table 7
Compressive damage parameters.

Tensile stress (MPa)	2.23	1.81	1.40	1.14	0.95	0.83	0.52	0.39	0.275
Cracking strain (%)	0	0.004	0.008	0.012	0.016	0.019	0.034	0.049	0.078
Damage factor d_t	0	0.396	0.627	0.750	0.820	0.864	0.949	0.972	0.988

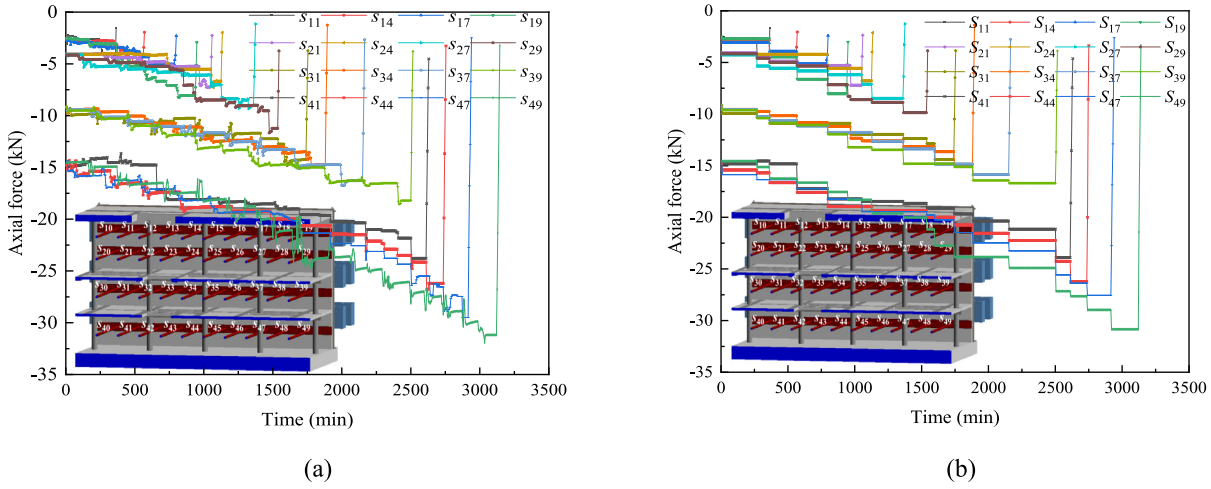

Fig. 10. Variation in the axial forces of the balance props. (a) Measured axial force data, and (b) axial force finite element simulation data.

props from left to right. The initial values of the balance props in the four layers are 2.54, 4.05, 9.08, and 14.56 kN.

The initial values of the balance props s_{11}, s_{12}, s_{13}, and s_{14} are all −2.54 kN. After the unloading of s_{10}, the axial forces of the surrounding balance props increase. As s_{11} is the closest to s_{10}, s_{11} experiences the greatest increase in axial force, with the axial force of s_{11} increasing from −2.54 to −4.12 kN. After s_{11} is unloaded, the cumulative axial force of s_{14} increases from −3.19 to −3.67 kN. After s_{14} is unloaded, the cumulative axial force of s_{17} increases from −3.84 to −4.34 kN. After s_{17} is unloaded, the cumulative axial force of s_{19} increases from −7.05 to −8.03 kN.

Owing to the increases and decreases in the axial forces after the unloading of the upper balance props, after the unloading of s_{1j}, the axial force of s_{2j} varies only slightly. The initial axial force values of the balance props s_{21}, s_{22}, s_{23}, and s_{24} are −4.07, −4.08, −4.05, and −4.15 kN, respectively. After unloading s_{20}, the cumulative axial force of s_{21} increases from −5.24 to −7.10 kN. After unloading s_{21}, the cumulative axial force of s_{24} increases from −5.53 to −6.68 kN. After unloading s_{24}, the cumulative axial force of s_{27} increases from −7.03 to −8.26 kN. After unloading s_{27}, the cumulative axial force of s_{29} increases from −8.99 to −9.55 kN.

The changes in the axial forces of the balance props in the third and fourth layers are similar to those of the balance props in the previous two layers. Given the scope of this work, we do not elaborate upon this concept further here. In summary, the changes in the axial forces of the balance props indicate that as the previous balance props are unloaded, the axial forces of the surrounding balance props at the unloading position increase. As the initial axial forces of the balance props from the first layer to the fourth layer increase, the unloading of the previous balance props has a greater effect on the axial forces of the subsequent balance props. The increase in the axial forces of the balance props is negatively correlated with the distance to the previous balance props and positively correlated with the axial forces of the previous balance props at the time of unloading.

6.2 Damage process analysis

Owing to the limitations of the experimental devices on both sides of the model and the top counterweights, it is not possible to directly observe or measure the cracking and development of the metro station structure's sidewalls and top slab during the loading process. However, the structural failure characteristics can be reflected by observing the initiation and development of the internal cracks in the concrete structure. Figure 11 shows the cracks in the right sidewall of the basement first floor under various construction conditions. Since the figure is large and difficult to annotate clearly, for ease of description, the corresponding crack diagrams for each condition were drawn via CAD.

On the basis of crack initiation, crack development, and the structural failure state, structural failure during the experimental loading process can be divided into four stages: no cracking, initial cracking, crack penetration, and local failure.

At pressures 0–4 times the soil pressure, no cracks are observed on the concrete surface, indicating that the structure is still in an elastic state. Compared with the finite element simulation results, at this stage, the overall tensile and compressive damage values of the metro station are relatively small, and the structure does not develop cracks. This stage is therefore classified as the no-crack stage (Stage I).

At pressures 4.5–8.5 times the soil pressure, no cracks appear inside the structure's sidewalls. However, some fine cracks begin to appear on the surface of the concrete floor slabs. The cracks are at the corners and middle areas of the excavation openings. At this point, the cracks are small, with the longest crack being only 4.5 cm in length and the maximum crack width being 0.02 mm, as shown in Fig. 12(a), (b), and (c). The reinforcement in the crack locations experiences increased stress, as shown in Fig. 12(d). A comparison of the experimental results and finite element calculations reveals that the crack distributions of the experimental model and finite element model are consistent. The finite element simulation results reveal that the cracking of the floor slab in the station structure is primar-

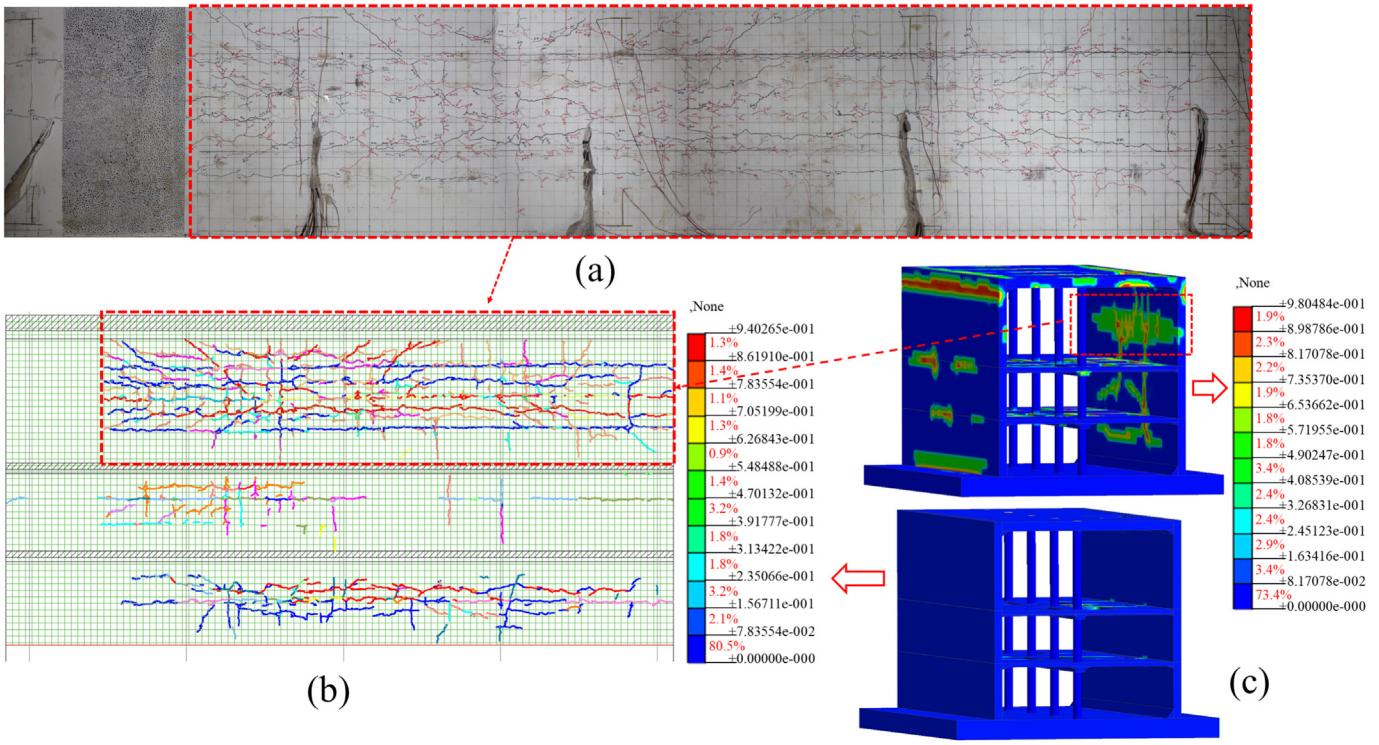

Fig. 11. Crack diagram of the right sidewall of the basement first floor. (a) Test results of crack distribution on side walls, (b) simulation results of crack distribution on the side wall, and (c) simulation results of tensile and compressive damage to side walls.

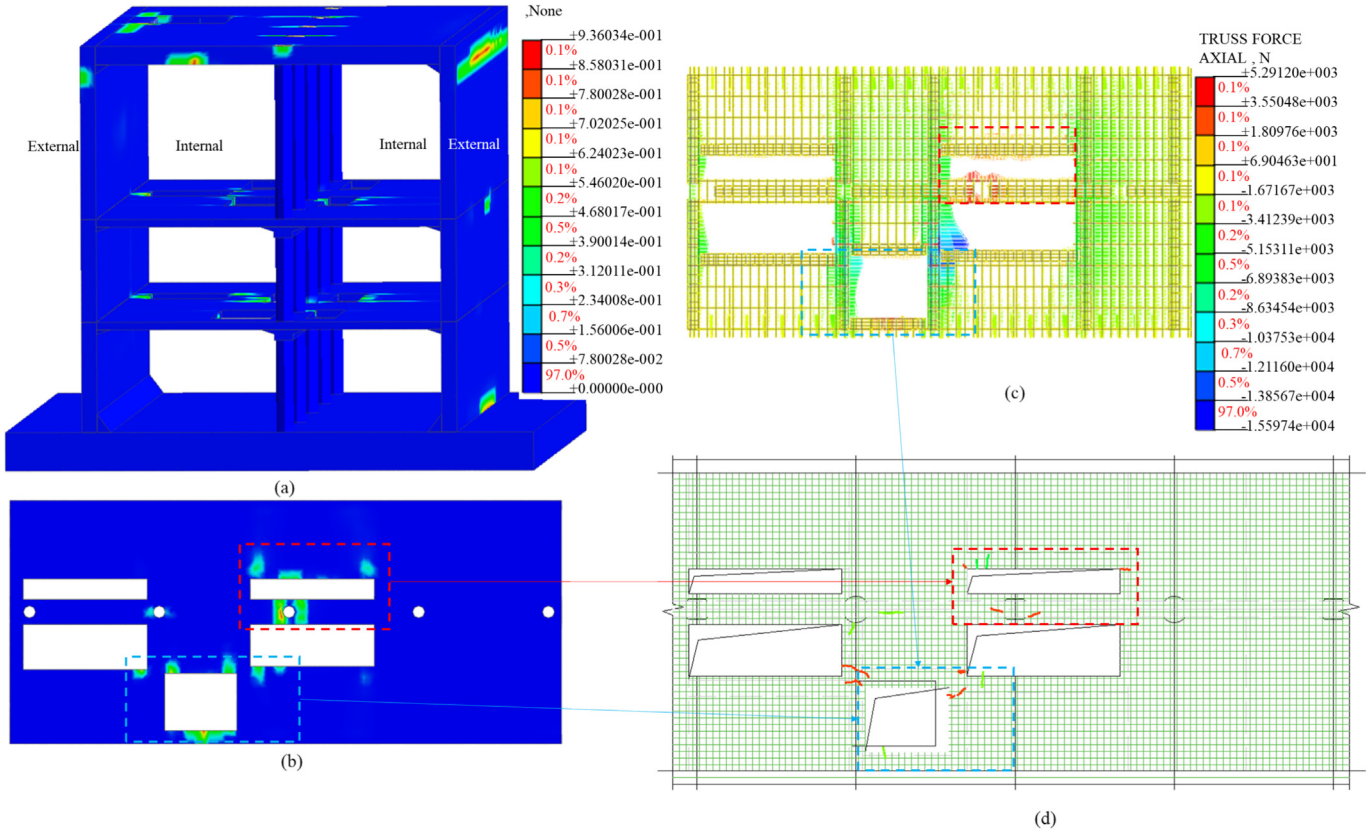

Fig. 12. Crack development (Stage II). (a) Overall station model, (b) tensile damage of the basement second-floor slab, (c) crack diagram of the basement second-floor slab, and (d) reinforcement axial force diagram.

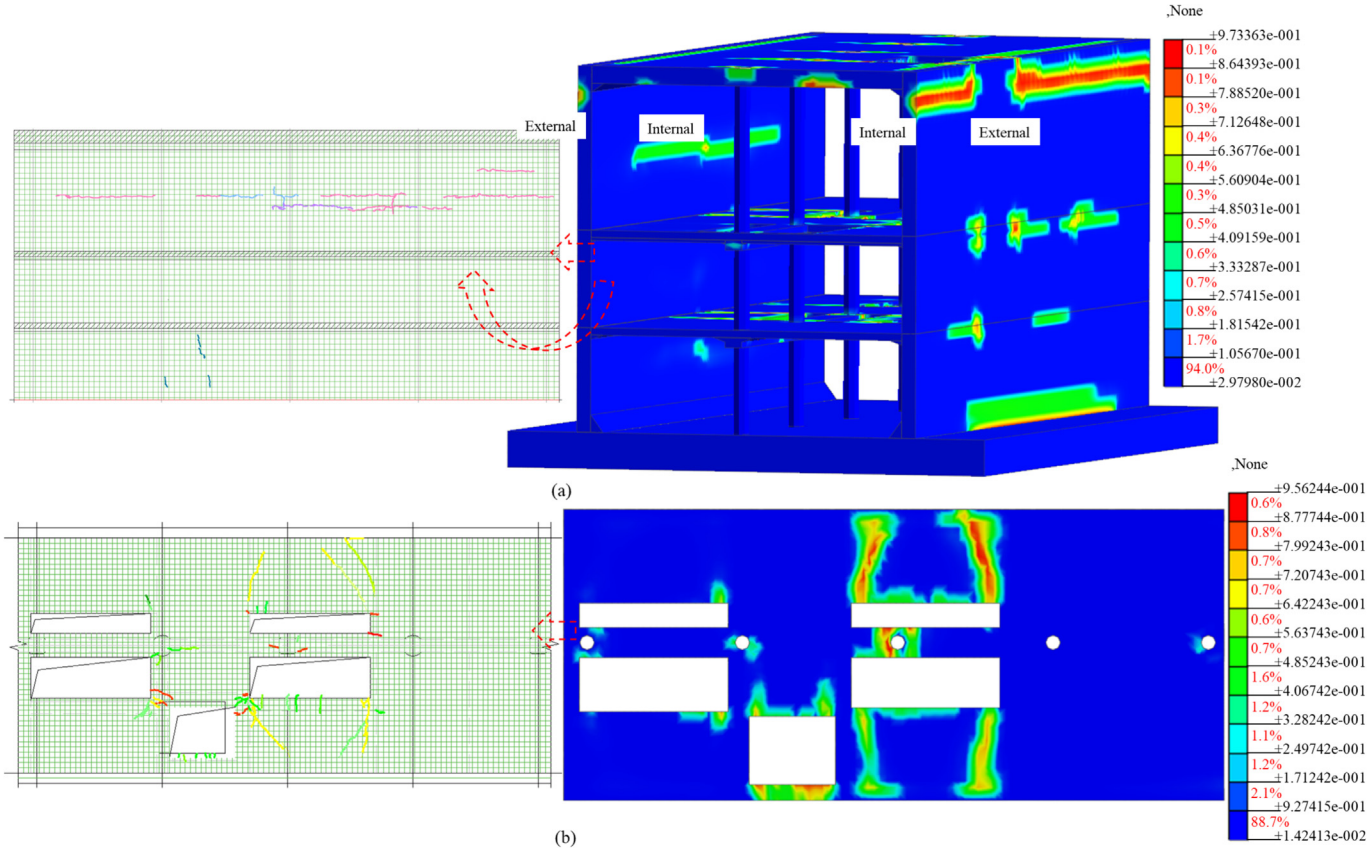

Fig. 13. Crack development (Stage III). (a) Side wall cracking and damage status, and (b) cracking and damage status of the basement second-floor slab.

ily due to tensile damage, with increased stress in the reinforcement at the crack locations. At this stage, the structure is still in an elastic state overall, but plastic zones are beginning to form. This stage is classified as the initial cracking stage (Stage II).

The crack distribution at pressures 9–12.5 times the soil pressure is shown in Fig. 13. The cracks from the model test clearly indicate that the cracking rate accelerates during this stage. A through-thickness transverse crack appears at the middle of the internal sidewall of the basement first floor of the metro station, with numerous small oblique cracks surrounding the through crack, as shown in Fig. 13(a). As shown in Fig. 13(b), cracks at the corner of the excavation opening and the middle area of the excavation hole develop obliquely along the width of the floor slab. Multiple cracks are distributed at the center of the

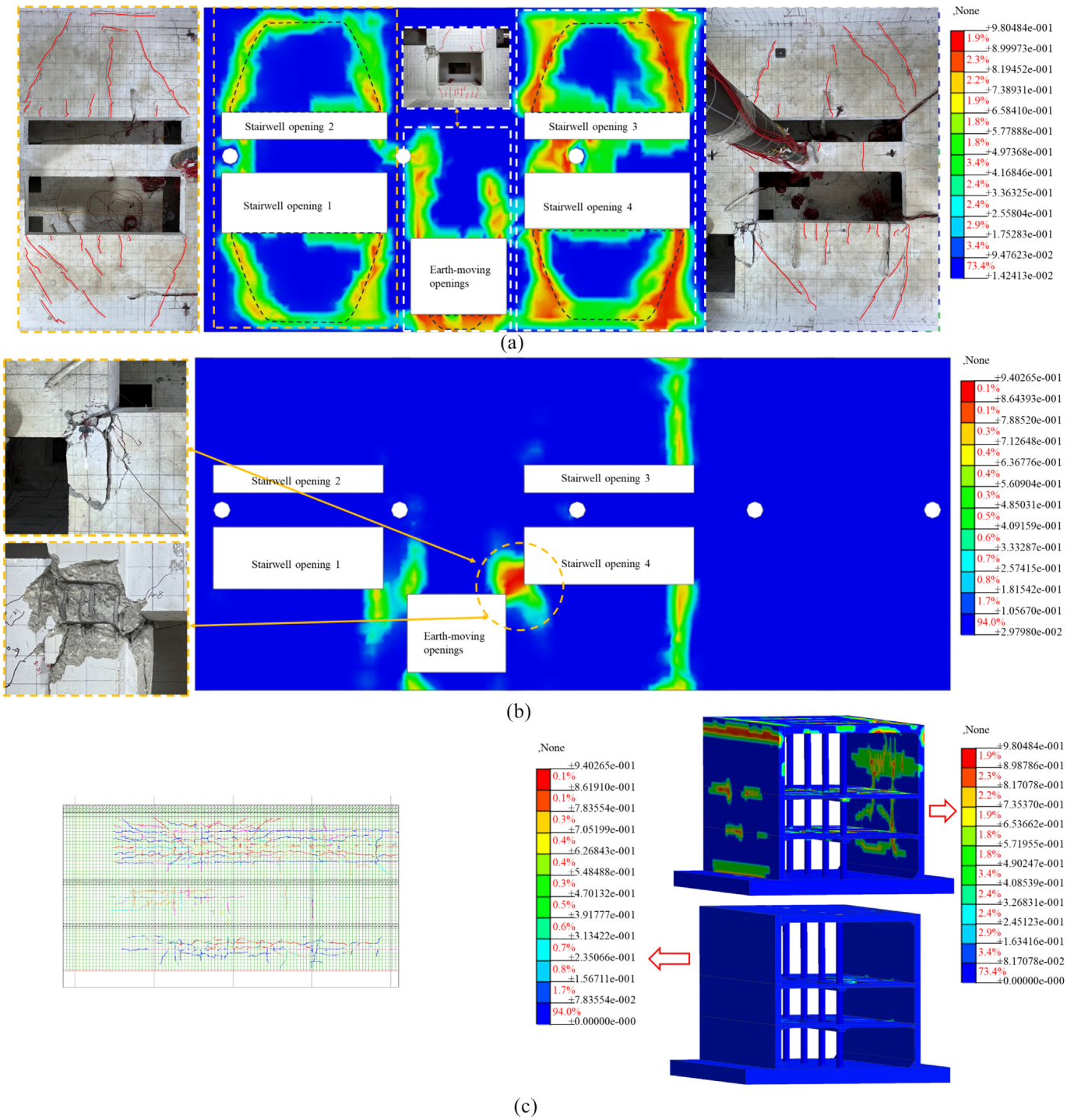

Fig. 14. Crack development (Stage IV). (a) Cracking and damage status of the basement second-floor slab, (b) cracking and damage status of the basement third-floor slab, and (c) side wall cracking and damage status.

floor slab, and these cracks are close to becoming interconnected. Compared with the finite element simulation results, in this stage, compressive damage dominates, whereas tensile damage remains at a relatively low level. The region where the station structure is in an elastic state shrinks, whereas the plastic zone expands. This stage is classified as the crack penetration stage (Stage III).

Figure 14 shows the final stage (Stage IV) of the experimental loading process, corresponding to pressures 13.0–15.5 times the soil pressure. As shown in Fig. 14(a), and on the basis of the experimental observations, at pressures 13.0–14.5 times the soil pressure, with increasing water and soil pressure, cracking sounds begin to occur inside the structure. The crack propagation speed accelerates, and the concrete at the excavation hole and stairwell openings of the basement second-floor slab begins to fracture. At pressures 14.5–15.5 times the soil pressure, the cracking sounds from the internal concrete intensify. Significant tensile damage occurs at the stairwell openings (1, 2, 3, and 4) and at the excavation holes along the width of the openings. The main tensile damage area takes the shape of a horseshoe. The crack development observed during the experiment shows that from the corners of the openings, numerous oblique primary cracks develop transversely, with many new oblique cracks appearing beside the primary cracks. Numerous fine vertical cracks appear transversely along the center of the opening, with the crack length decreasing gradually along the longitudinal direction from the center of the span.

Figure 14(b) clearly shows that the concrete at the excavation hole and stairwell openings on the basement second-floor slab experiences compressive crushing and spalling, with the reinforcement becoming exposed. The exposed reinforcement clearly shows signs of yielding deformation, indicating localized structural damage. This stage is classified as the local damage stage.

Figure 14(c) shows that the cracks in the station sidewalls are caused primarily by tensile forces. At this point, cracks are distributed throughout the sidewalls (Stage IV).

7 Discussion

In this study, we developed a loading device that considers various water—soil pressures and analyzed the damage and failure processes of a subway station model under different water—soil pressures. However, research on loading devices is still in its early stages, and many issues require further investigation. For example, the effects of pore water pressure and vibration loads on structural stress and damage cannot be considered with existing loading devices. Owing to constraints related to the experimental period and testing conditions, we simulated only the key excavation process via the cover excavation reverse construction method in this experiment. Moreover, we could not fully replicate the time-varying characteristics of the loads during the entire cover excavation reverse construction process. Considering the safety of model lifting during and after the experiment, the bottom slab was not reinforced according to similarity theory, which significantly affects the overall stiffness of the bottom slab and the sidewalls of the basement third floor. When simulating the interaction between the soil and structure, a uniform sandy soil was used as the layered fill material, without considering the stratification and inhomogeneity of the in situ soil. Furthermore, no constraints at the ends of the structure were considered.

8 Conclusions

(1) Considering the equivalence of water and soil pressure loads, an excavation unloading device and an external soil pressure graded loading device for subway stations created via cover excavation and reverse construction processes were developed. This approach enabled the simulation of the excavation and failure processes of the subway station, providing insights into the stress and failure characteristics of the station.

(2) During the simulation of the construction stage, with the external water and soil pressure remaining constant, as the balance props were unloaded, the axial force of the surrounding balance props increased at the unloading position. As the initial axial force of the balance props increased, the effect of unloading the preceding balance props on the axial force of the subsequent balance props became more significant. The increase in the axial force of the balance props was negatively correlated with the distance to the preceding balance props and positively correlated with the axial force of the preceding balance props at the time of unloading.

(3) During the bearing capacity stage, on the basis of the incremental soil pressure load and the corresponding crack initiation, development, and structural failure states, the model failure process was divided into four stages. These stages were classified as follows: pressures 0–4 times the soil pressure, which was the no-crack stage; pressures 4.5–8.5 times the soil pressure, which was the initial cracking stage; pressures 9–12.5 times the soil pressure, which was the crack penetration stage; and pressures 13–15.5 times the soil pressure, which was the local damage stage. Cracks in the station structure first appeared at the corners and the center of the excavation openings. The first through-thickness transverse crack appeared in the middle of the basement first-floor wall. Cracks at the corners and the center of the excavation openings developed obliquely, with the cracks forming an overall horseshoe shape. Localized damage first occurred at the corners, where the concrete spalled, exposing the reinforcement.

Data availability

The data that support the findings of this study are available from the corresponding author upon reasonable request.

CRediT authorship contribution statement

Dongbo Zhou: Writing – original draft, Validation, Formal analysis, Visualization, Investigation, Data curation. **Yuan Mei:** Supervision, Funding acquisition, Writing – review & editing, Methodology, Conceptualization. **Xin Ke:** Validation, Visualization. **Ziyang Liu:** Resources, Validation. **Wangyang Xu:** Resources.

Declaration of competing interest

The authors declare that they have no known competing financial interests or personal relationships that could have appeared to influence the work reported in this paper.

Acknowledgement

The research described in this paper was financially supported by the National Natural Science Foundation of China (Grant No. 52178302) and the Key R&D Projects in Shaanxi Province (No. 2020SF-373).

References

Chang, Y., Wan, L., Mo, D., Hu, D., & Li, S. (2022). Tensile damage of reinforced concrete and simulation of the four-point bending test based on the random cracking theory. *Computer and Concrete*, *30*(4), 289–299.

Chen, Y., Jia, P., & Ji, X. (2021). Investigation into the performance of a covered top-down pit-in-pit deep excavation in shenzhen soil-rock mixed strata. *Arabian Journal for Science and Engineering*, *46*(11), 10419–10437.

Du, X., Li, Y., Dong, X., & Han, K. (2024). Large deformation induced soil pressure changes in a loess tunnel. *Engineering Failure Analysis*, *163*, 108568.

Du, Y., Fu, S., & Zhao, Y. (2022). Theoretical calculations and field measurements of the Earth pressure in the jinci tunnel. *Soil Mechanics and Foundation Engineering*, *59*(1), 77–84.

Elbelbisi, A., El-Sisi, A., Elgholmy, L., Helal, Z., Elemam, H., Saucier, A., & Salim, H. (2024). Experimental study on non-load bearing multi-span sandwich wall panels for blast mitigation. *Journal of Building Engineering*, *98*, 110968.

Fu, Q., & Li, L. (2020). Vertical load transfer behavior of composite foundation and its responses to adjacent excavation: centrifuge model test. *Geotechnical Testing Journal*, *44*(1), 191–204.

Ganesh, P., & Ramachandra Murthy, A. (2023). Flexural fatigue strains of constituent materials in strengthened RC beams with UHPC strips. *International Journal of Fatigue*, *167*, 107351.

Guo, P., Lei, G., Luo, L., Gong, X., Wang, Y., Li, B., Hu, X., & Hu, H. (2022). Soil creep effect on time-dependent deformation of deep braced excavation. *Advances in Materials Science and Engineering*, *2022*(1), 5655592.

Jamsawang, P., Jamnam, S., Jongpradist, P., Tanseng, P., & Horpibulsuk, S. (2017). Numerical analysis of lateral movements and strut forces in deep cement mixing walls with top-down construction in soft clay. *Computers and Geotechnics*, *88*, 174–181.

Jin, Y., Di, H., Zhou, S., Liu, H., Wu, D., & Guo, H. (2024). Effects of active axial force adjustment of struts on support system during pit excavation: Experimental study. *Journal of Geotechnical and Geoenvironmental Engineering*, *150*(5), 4024027.

LeBlanc, J. M., Brachman, R. W. I., & Zarpeima, A. (2024). Design-truck ultimate limit states of buried modular polymer stormwater collection structures. *Canadian Geotechnical Journal*, *61*(7), 1368–1384.

Ma, X., & Cao, M. (2024). Evaluation of deformation for two-dimensional (2D) and three-dimensional (3D) braced excavation in clays with centrifuge modelling and numerical analysis. *Canadian Geotechnical Journal*, *61*(12), 2785–2805.

Ma, X., & Liu, L. (2023). Fatigue properties of RC beams reinforced with ECC layer and steel plate. *Construction and Building Materials*, *372*, 130799.

Marzec, I., & Tejchman, J. (2022). Experimental and numerical investigations on RC beams with stirrups scaled along height or length. *Engineering Structures*, *252*, 113621.

Mei, Y., Zhou, D., Wang, H., Ke, X., Liu, Z., Tian, X., & Wang, Z. (2024). Study on carbon emission calculation during the materialization phase of subway stations and comparative analysis of carbon emissions from various construction methods. *Case Studies in Construction Materials*, *21*, e03923.

Meral, Ç., Temel, B. A., & Başaga, H. B. (2024). Choosing the right construction method: A comparative study of cost and timeline for top-down and bottom-up approaches. *Buildings*, *14*(8), 2381.

Pham, K. V. A., Kim, Y.-N., Woo, S., Kim, S. J., Lee, G., & Lee, K. (2024). Experimental-FEA investigation of the structural performance of steel box connector in precast concrete connection. *Journal of Building Engineering*, *95*, 110077.

Shi, G., Yang, X., Sun, J., Tao, Z., & Sousa, L. R. E. (2024). Experimental study on the control characteristics of the negative poisson's ratio structural anchor cable on the large deformation of rainfall-induced landslide. *Bulletin of Engineering Geology and the Environment*, *83*(4), 134.

Sun, S., Guo, Y., Gui, P., Xing, L., & Mei, K. (2023). Flexural behaviour of steel–basalt fibre composite bar-reinforced concrete beams. *Engineering Structures*, *289*, 116246.

Sun, Y., Che, Y., Gu, Z., Wang, R., & Fan, Y. (2022). Measured structural response of a long irregular pit constructed using a top-down method. *Geomechanics and Engineering*, *31*, 489–503.

Vuong, T.-N.-H., Nguyen, T.-K., Nguyen, D.-L., Le, H.-V., & Tran, N.-T. (2023). Fiber fraction-dependent flexural behavior of high-performance fiber-reinforced concrete under static and repeated loading. *Journal of Building Engineering*, *79*, 107808.

Wang, S.-Q., Feng, D.-C., & Wu, G. (2022). Design and bearing capacity test of prefabricated high-strength thin concrete segments for reinforcing underground box culverts. *Engineering Failure Analysis*, *142*, 106844.

Wang, Y., Pan, X., Xu, H., Liu, J., Li, P., He, L., & Zhang, W. (2024a). Characteristics analysis for high-rise buildings during top-down construction. *Journal of Civil Engineering and Management*, *30*(4), 326–342.

Wang, Y., Zhang, D., Zhao, J., Du, Q., & Mubizah, R. (2024b). Seismic behavior of exterior joint of CFDST column to steel beam with RC slab. *Journal of Building Engineering*, *97*, 110861.

Xu, X., Zheng, Y., Lan, X., Pan, J., & Wen, Y. (2024). Numerical simulation analysis of controlling settlement by water-resisting curtain combined with recharge in deep foundation pit. *Journal of Civil Engineering and Management*, *30*(7), 566–580.

Xue, Y., Dai, W., Wang, X., Li, C., & He, J. (2024). Development of OFDR-based inclination sensor for deformation measurement of foundation pile. *Measurement*, *231*, 114618.

Zhang, J. (2024). Pounding induced overturning resistance of FPB-isolated structures considering soil-structure-interactions. *Soil Dynamics and Earthquake Engineering*, *177*, 108416.

Zhang, M., Xie, Z., & Li, P. (2022). Bearing capacity and failure behavior of disconnectable coupling joint with double row wedges (DCJD) used in the prestressed internal bracing. *Underground Space*, *7*(4), 498–513.

Zhang, Q., Hu, J., Wang, J., He, P., Hou, L., Lin, P., & Song, S. (2021). Study on the mechanical behavior of a foundation pit retaining structure adjacent to the pile foundation of a subway station. *Environmental Earth Sciences*, *80*(20), 704.

Zhang, S., Gao, J., Liu, C., Li, P., Yang, Z., & Lu, X. (2024). Model test on the collapse mechanism of subway tunnels in the soil-sand-rock composite strata. *Engineering Failure Analysis*, *162*, 108356.

Zhang, T., Li, X., Hou, Z., Chen, Q., Fang, Y., & Sun, W. (2025). An improved damage plastic model for RC structure FE modelling under cyclic loading conditions. *Engineering Structures*, *322*, 119135.

Zheng, X., Zhang, C., Gao, S., & Wang, F. (2023). Predicting the bond strength between steel wire and mortar based on interfacial porosity and shrinkage. *Journal of Building Engineering*, *68*, 106188.

Zhou, D., Mei, Y., Ke, X., Liu, Z., & Xu, W. (2024). Study on the structural behavior and reinforcement design of openings in subway station floor slabs. *Journal of Building Engineering*, *98*, 110994.

Zhou, Y., Ye, Z., Zhao, D., Huang, Z., & Yang, L. (2023). Static and multi-impact performances of RC beams strengthened with large rupture-strain FRP composites. *Composite Structures*, *316*, 117053.

Zhuang, H., Yang, J., Chen, S., Dong, Z., & Chen, G. (2021). Statistical numerical method for determining seismic performance and fragility of shallow-buried underground structure. *Tunnelling and Underground Space Technology*, *116*, 104090.